ANALYTICAL AND SIMPLIFIED NUMERICAL APPROACHES OF FRCM PIPES

Ernest Bernat-Maso[a,c*], Luis Mercedes[b] and Lluís Gil[a]

[a] Strength of Materials and Structural Engineering Department, Universitat Politècnica de Catalunya. C/ Colom 11, TR45. 08222 Terrassa

[b] Laboratory for the Technological Innovation of Structures and Materials (LITEM), Universitat Politècnica de Catalunya. C/ Colom 11, TR45. 08222 Terrassa

[c] Serra Húnter Fellow

[*] Corresponding author. ernest.bernat@upc.edu

Abstract

Despite the well-known advantages of fabric-reinforced cementitious matrix (FRCM), few applications of this composite material have been proposed apart from structural strengthening. To exploit material corrosion resistance, seven FRCM pipes were produced with mortar and dry concrete matrixes. They were experimentally tested under diametral compression configuration, and their cracking load and load-bearing capacity were compared with both analytical and numerical simulations results, which indicated the better accuracy (between 10% and 16% of relative error) of the proposed analytical approach, proving the efficiency of the latter as a calculation tool for this innovative structural application of FRCM.

Keywords

A. Fabrics/Textiles; B. Analytical modelling; C. Finite Element Analysis; D. Mechanical testing; E. Pipe

1. Introduction

Textile-reinforced mortar (TRM), fabric-reinforced cementitious matrix (FRCM), and textile-reinforced concrete (TRC) are some of the technological names representing composite materials with fibre meshes embedded into inorganic matrixes. 'FRCM' shall be used to represent the abovementioned composite materials hereinafter for simplicity, although slight differences may occur in terms of the material definition for each of them.

Studies to develop new structural elements based on these composite materials started in the 1980s, in which reinforcing fibre meshes were used to replace short fibres in mortars. The pioneer study by Gardiner et al. [1] is a primary example thereof. However, this technology has evolved to the practical application as strengthening materials for existing masonry (see [2–5]) and concrete structures (see [6–8]), resulting in increased strength and deformability (see [9]). These results oriented following researches on the material characterisation of the tensile response (see [10–12]).

At the beginning of the 21st century, researchers have attempted to develop new structural elements based on FRCMs. They focused on the effect of mesh geometry on the strength of the resulting structural elements (see Peled et al. [13]) and the stress analysis of linear elements. Recently, El Messiry et al. [14] analysed the effect of mesh spacing on the composite material strength, whereas Han et al. [15] extended the study to investigate the effect of the geometric definition of three-dimensional meshes on FRCM strength.

Although the industrialised production of FRCM structural elements does not exist, to the authors' knowledge, two main developments have been reported: pultrusion of inorganic matrix-textile-reinforced elements and prestressing of FRCMs. Regarding the former, the effects of mesh geometry, concrete properties, and pressure concrete was subjected to, the influence

of the type of fibres and knitting process and the possibility of embedding multiple textile layer, even from different fibres in a single hybrid composite, they were analysed in relation to the mechanical performance of pultruded FRCMs (see [16–18]). Furthermore, effect of impact loads on pultruded TRC elements has been investigated by Butnariu et al. [19].

Regarding the prestressing of FRCMs, some authors regarded it as an initial requirement for the durability of FRCM structural elements. In addition, it enables an active compatibility between mesh and matrix. The tensile response of prestressed FRCMs has been studied (see [20–24]).

Mechtcherine et al. [25] recompiled a reference of TRC applications. Focusing on pipe production using FRCMs, researchers (see [17]) have proposed using multiple mesh layers and fluid mortar, similar to the FRP (Fibre Reinforced Polymer) technology, in which a numerous fibres are embedded into a matrix penetrating between them. Similarly, Quadflied et al. [26] suggested using the electrical conductivity of fibres to auto-detect leakage pipes, but the study was focused more on the material than on the structure.

However, the abovementioned studies focused on producing FRCM structural elements using fluid mortar/microconcrete, whereas the current practice in pipe production uses dry concrete. Only the study performed by Peyvandi et al. [27] focused on using dry concrete with short fibres (no textile) to partially replace steel reinforcement in the production of large concrete pipes with increased durability and shear strength. Brameshuber et al. [28] proposed using a polymer pipe as a collaborating support to produce multiple-layer textiles and fluid concrete FRCM pipes, resulting in hybrid structural elements. Finally, Helbig et al. [29] proposed using multilayer FRCMs to produce pipes.

It is clear that studies regarding FRCM pipe production are rare and those regarding the analytical or numerical calculation of these elements are not available. To solve this calculation

problem, the model included in ACI 549.4R-13 [30] or the ACK model [31] are first proposed as initial references to analyse FRCM composite strengthening and FRCM tensile material response, respectively, among others. Regarding the numerical simulation of FRCMs, two main research directions are defined: the simulation of FRCM material as it is (see [32–34]) and the simulation of FRCM strengthening applications on concrete (see [35–38]) or masonry (see [39–41]) structures.

Hence, the main aim of the present study is to study the structural response of mortar and concrete FRCM pipes from experimental, analytical, and simulation approaches and subsequently compare them. The achievement of this goal may contribute to the future design of concrete FRCM pipes, considering the well-stated data and calculation tools for mortar FRCM elements. Therefore, maintaining the current concrete consistency (minimum slump) for future industrial productions of concrete FRCM pipes is the economical requirement that sets the context of the current study.

2. Materials and methods

2.1. Materials

2.1.1. Matrixes

Two matrixes were used to produce FRCM pipes. The first matrix was an auto-levelling (fluid) mortar (*M*) that included fibres and additives, which enabled a good impregnation of fabric. For comparison purposes, the selected mortar was the same as that in a previous study [24]. This mortar was classified as CT-C20-F5 according to EN 13813 [42], and it was characterised by its slump value of over 200 mm. The maximum recommended mortar thickness was 10 mm.

The second matrix was a dry consistency concrete with additives (*C*), which was selected to represent the concrete used to produce large industrialised reinforced concrete (RC) pipes. The

consistency of this concrete (the maximum slump was 20 mm; therefore, the slump class was S1 according to BS EN 12350-2 [43]) enabled pipes to be unmoulded immediately after they were cast and compacted by vibration. This requirement must be maintained such that future alternatives can be proposed based on replacing steel grids by fibre fabrics without extending the time that moulds are used to produce a single specimen.

The compressive strength of the mortar was obtained from two axial experimental tests on unreinforced pipe elements with the same geometry than the reinforced ones to account for the imperfections associated with the casting process of thin elements. The compressive strength of the concrete was obtained from an industrial supplier. Using the formulation presented in article number 39 of the Spanish concrete code [44], the elastic modulus and tensile strength of both mortar and concrete were calculated from the corresponding compressive strength. The mechanical properties are summarised in Table 1.

Matrix	***Compressive strength, f_{ck} (MPa)***	***Tensile strength, f_{ct} (MPa)***	***Elastic modulus, E_c (GPa)***
Mortar (M)	11.2	1.78	32.0
Concrete (C)	30.0	2.03	48.8

Table 1. Mechanical properties of matrixes

2.1.2. Reinforcing fabrics

Three different fabrics were used in the experimental campaign. A 10-mm-spacing bidirectional carbon fabric (*Cf*) was used to reinforce mortar pipes, whereas larger-spacing glass fabrics (GF) and carbon fabric (*CF*) were used to reinforce one large-scale concrete pipe each. Different types of carbon fabrics were required for mortar and concrete pipes because the small spacing between tows of the *Cf* mesh prevented concrete particles to pass through. Similarly, the maximum curvature possibilities of the *CF* mesh impeded the production of mortar pipes with the intended geometry, within the maximum mortar thickness of 10 mm. Producing mortar and

concrete specimens reinforced with both carbon fabrics was necessary to study concrete FRCMs from the response of mortar FRCMs, which has already been investigated. From a previous study [24], it was demonstrated that better results were obtained using carbon FRCMs than glass FRCMs; therefore, glass fabric was only considered for the full-scale concrete specimen.

It is noteworthy that the *CF* is not balanced in both directions. The geometric and mechanical properties of the meshes and fibres are summarised in Table 2. The ultimate tensile force (F_m^{ult}) of the *Cf* was calculated from experimental tensile strength tests on the same combination of mortar and fabric (see [24]). The elastic modulus of the fabrics (E_m) was calculated (see Eq.1) from the ultimate tensile force of the fabric (F_m^{ult}), equivalent thickness (t_{tex}), and ultimate strain of fibres (ε_m^{ult}), which were provided by the manufacturer.

$$E_m = \frac{F_m^{ult}}{t_{tex} \cdot \varepsilon_m^{ult}} \qquad \textit{(Eq.1)}$$

The remaining values were directly provided by suppliers.

	Property	***Units***	***Carbon fabric for mortar pipes (Cf)***	***Carbon fabric for concrete pipes (CF)***	***Glass fabric for concrete pipes (GF)***
Fibres	*Ultimate tensile strength*	$f_{fib,u}$ *[MPa]*	4800	2000	2000
	Ultimate strain	ε_m^{ult} *[%]*	1.80	0.76	1.55
Fabric	*Fibre orientation*		Bidirectional	Bidirectional	Bidirectional
	Roving separation (mm)	s_{tex} *(mm)*	5	46/41	38
	Equivalent thickness	t_{tex} *(mm)*	0.047	0.045/0.040	0.115
	Ultimate tensile force	F_m^{ult} *[kN/m]*	59	80.75/79.9	125
	Young modulus	E_m *[GPa]*	69.7	236.1	70.1
	Polymer coated rovings		No	Yes	Yes

Table 2. Mechanical and geometric properties of fibres and fabrics

2.2. Specimens

2.2.1. Fabric-reinforced mortar pipes

Four mortar pipes were produced and tested. Two of them with no reinforcement (*M01* and *M02*) and the other two reinforced with one layer of *Cf* (*MCf1* and *MCf2*) placed at the centre of the wall thickness. The overlap of the fabric was 20 mm. Two concentric PVC (polyvinyl chloride) pipes were used as the mould. A specific bottom cap was designed to set the concentric position of the PVC pipes and to centre the carbon fibre fabric (see Figure 1a). No spacers were necessary because of the short length of the specimens and the fabric stiffness. Mortar was cast into the mould containing the fabric. No vibration was necessary because of the fluid consistency of the mortar. The specimens' dimensions are summarised in Table 3. These specimens were produced in the LITEM-Polytechnic University of Catalonia laboratory. Specimens were unmoulded one week after casting when the required strength was attained. Subsequently, they were cured at indoor air conditions (20 °C ± 4 °C, 65% ± 10% humidity) without requiring additional wetting for three additional weeks before testing. Because of their reduced size, the specimens could be handled manually.

2.2.2. Fabric-reinforced concrete pipes

Three concrete pipes were produced and tested: one with no reinforcement (*C0*), one reinforced with *CF* fabric (*CCF*), and one reinforced with *GF* fabric (*CGF*). The fabrics were placed at the centre of the wall thickness (Figure 1b). Concrete spacers were placed at both sides of the fabric to set its position with respect to the internal and external formworks. This was necessary because the fabric tended to move from the intended position owing to the consistency of concrete. The CF was placed with the orientation that yielded the best performance following a circumferential direction. Dry concrete was cast from the top of the formwork, and the full structure including the mould was vibrated during casting. A concrete vibrator was introduced from the top part to assure an effective compaction. The pipes were unmoulded immediately after they were cast (see Figure 1c). The specimens were cured at indoor air conditions (15 °C ±

5 °C, 70% ± 15% humidity) without requiring additional wetting for four weeks before moving them from the producer company, SORIGUÉ S.L. facilities, to the testing laboratory. A crane was used to manage the concrete specimens. The specimens' dimensions and detailed test results are summarised in Table 3. Cracking force is the load applied when the first crack appeared during the tests. The maximum force corresponds to the load-bearing capacity of the pipe.

Specimen	*Matrix*	*Fabric*	*External diameter, De (mm)*	*Internal diameter, Di (mm)*	*Length (mm)*	*Cracking force, F_{fis} (N)*	*Maximum force, F_{max} (N)*
M01	*M*	---	118.2	90.1	239	2034	---
M02	*M*	---	118.6	89.9	239	1651	---
MCf1	*M*	*Cf*	119.2	90.5	239	1874	1979
MCf2	*M*	*Cf*	118.5	90.3	235	1596	1685
C0	*C*	---	615	493	785	30095	56044
CGF	*C*	*GF*	615	493	795	21286	98366
CCF	*C*	*CF*	615	495	797	30318	93108

Table 3. Properties of the FRCM pipe specimens and experimental results

(a) (b) (c)

Figure 1. Carbon mesh in the bottom cap for mortar specimens (a), positioning of glass fibre mesh into the mould for concrete pipes (b), and immediately unmoulding pipe, with interior formwork removed (c)

2.3. Experimental tests

The specimens were subjected to diametral compression tests. Tests were performed under displacement control at a constant ratio of 5 mm/min. Load was applied with a 50 kN range electromechanical press and data was acquired at 5 Hz for mortar specimens. An oleo-hydraulic 300 kN range actuator and a 50 Hz data acquisition rate was used for the concrete specimens. A steel load distribution beam (250-mm-long IPE 120 for mortar specimens and 1000-mm-long HEB 200 for concrete specimens) was placed between the load cell and the pipe. The mortar

specimens were supported on a continuous 2-mm-thick rubber plate, whereas the concrete specimens were supported on two 20-mm-thick rubber pads separated by 40 mm to define a settling area. Between the load distribution beam and the mortar pipe, a 2-mm-thick continuous rubber strip was placed. Similarly, a 40-mm-wide and 20-mm-thick rubber strip was placed between the distribution load and concrete pipes. Finally, the lateral displacements of the concrete pipes were restrained at both sides at mid-height (307.5 mm from floor level) for safety reasons. These restraining points were in direct contact with the concrete pipe from the beginning of the test. Hence, these restrains affected the mechanical response of the tested concrete pipes compared with typical diametral compression tests, which do not include these restrains. The restrains were expected to limit lateral deformations and increase the failure load. Figure 2 shows the test setup for both types of specimens.

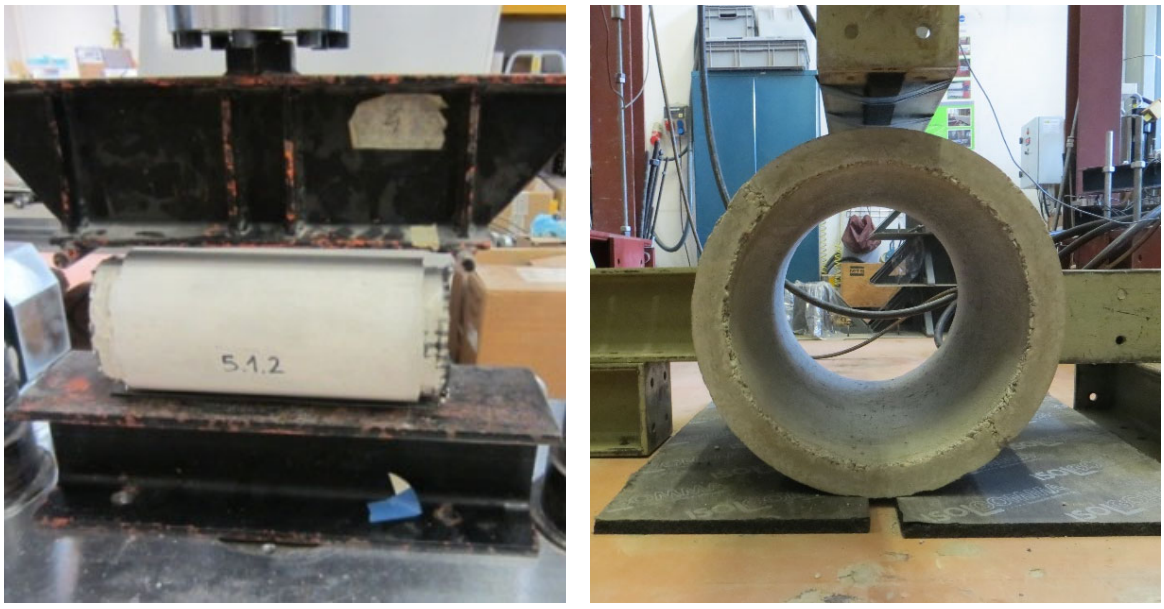

(a) (b)

Figure 2. Test setup for diametral compression tests on (a) mortar and (b) concrete pipes

2.4. Analytical approach

Cross-section normal forces and bending moment equilibrium equations (see Table 4) have been proposed to calculate both the cracking force (the load at which the first crack appeared because of reaching the tensile strength of mortar/concrete matrix) and ultimate load. The longitudinal cross section at the pipe top/bottom point and at the pipe mid-height lateral point were considered for calculation because the bending moment distribution indicated local or absolute maximum/minimum values in these positions. The equations used were the same as those for concrete design but a fibre mesh was considered as reinforcement instead of the typical steel grid. The fibre mesh reinforcement was assumed to exhibit a linear elastic behaviour until its tensile failure at the corresponding maximum load-bearing capacity and ultimate strain; both parameters are summarised in Table 2.

Figure 3 shows the stress/force distribution under the failure hypothesis of concrete crushing (b) or fibre mesh tensile failure (c). The equilibrium and compatibility equations for these two ultimate failure hypotheses as well as for the concrete cracking load calculation (last column) are summarised in Table 4.

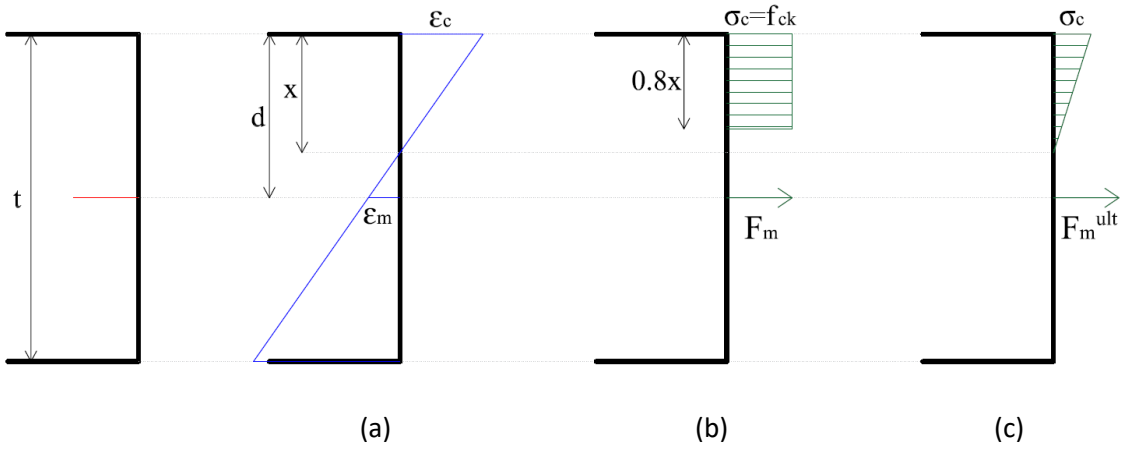

Figure 3. (a) Strain diagram, (b) stress diagram for concrete crushing hypothesis and (c) stress diagram for mesh tensile failure hypothesis and concrete behaving linear.

Regarding the variables in the equations shown in Table 4, *d* and *t* are the position of the fibre mesh and the total thickness of the pipe wall, respectively (see Figure 3); *R* is the radius (to mid-

thickness) of the pipe, which can be calculated from the data in Table 3; $\varepsilon_c^{ult} = 0.0035$ is the ultimate compressive strain of concrete. Finally, K_1 and K_2 are factors from the normal effort distribution (axial and bending moments). These may be obtained for different cases, as shown in Table 5.

Equation	***Concrete crushing***	***Mesh tensile failure***	***Concrete cracking***
Strain compatibility	$\varepsilon_m = \frac{\varepsilon_c^{ult} \cdot (d - x)}{x}$	$\varepsilon_c = \frac{\varepsilon_m^{ult} \cdot x}{d - x}$	$\sigma_c = \frac{x \cdot f_{ct}}{t - x}$
Tensile resulting force	$F_t = F_m = \frac{F_m^{ult} \cdot \varepsilon_m}{\varepsilon_m^{ult}}$	$F_t = F_m = F_m^{ult}$	$F_t = \frac{f_{ct} \cdot (t - x)}{2}$
Compressive resulting force	$F_c = 0.8 \cdot x \cdot f_{ck}$	$F_c = \frac{\varepsilon_c \cdot E_c \cdot x}{2}$	$F_c = \frac{\sigma_c \cdot x}{2}$
Bending moment equilibrium	$P = \frac{(d - 0.4 \cdot x) F_c}{K_1 \cdot R}$	$P = \frac{F_c \cdot \left(d - \frac{x}{3}\right)}{K_1 \cdot R}$	$P = \frac{\frac{\sigma_c \cdot x^2}{3} + \frac{f_{ct} \cdot (t - x)^2}{3}}{K_1 \cdot R}$
Force equilibrium	$F_c - F_t - K_2 \cdot P = 0$	$F_c - F_t - K_2 \cdot P = 0$	$F_c - F_t - K_2 \cdot P = 0$

Table 4. Equations for analytical approach

	No lateral restrained pipes		***Laterally restrained pipes***	
	Top/Bottom	*Mid-height lateral*	*Top/Bottom*	*Mid-height lateral*
K_1	0.3183	0.1817	0.1515	0.110607
K_2	0	0.5	0.4591	0.5

Table 5. K_1 and K_2 coefficients for different study cases

2.5. Numerical simulations

Numerical simulations were implemented with ANSYS® software using the static structural analysis package. The aim of these simulations was to provide a low-calculation cost and simplified approach for analysing structural elements composed of FRCMs. Analysis was based

on two-dimensional (2D) plain stress simplification. Moreover, some hypotheses were made regarding the geometry and materials, as explained below.

2.5.1. Geometry

First, the geometry definition considers that the failure mode of diametral compressed pipes is well known. It comprises the opening of four cracks: one in the top section, one in the bottom section, and two at the lateral mid-height sections. Hence, predefined failure planes (contacts) were defined at these sections.

Next, mesh rovings were not considered discretely and the fabric was assumed to be uniformly distributed along the pipe length; therefore, the equivalent thickness of the fibre mesh (t_{tec}) should have been used to represent the realistic equivalent geometry, as well as the mechanical properties summarised in Table 2. However, this approach would result in to mesh problems and excessive computational costs owing to the size difference between the 2D elements corresponding to the fabric and matrix, which was of three orders of magnitude. Additionally, the alternative of using line elements to represent the fabric, which may reduce meshing costs, rendered it more difficult to define the contacts required to represent the possible failure modes. In fact, this approach disabled the tensile mesh failure to be represented. Hence, a new geometry for the fabric was defined, in which its thickness was increased until approximately 3% of the pipe wall thickness. This was the minimum thickness for the objects representing the fabric that allowed meshing and problem solving in less than 15 min (Intel® Core™ i5-7500 CPU @ 3.40 GHz with 8GB RAM memory running Windows 10), while maintaining the results' convergence criteria associated with meshing refinement. This increased thickness of the objects representing the fabrics is called the virtual thickness (see Figure 4b). Because of the virtual thickness definition for the fabric representing objects, their mechanical properties were

modified to yield the same deformational response as that of real fabric and the maximum load-bearing capacity. These modifications were based on the ratio, *R* between the real fabric's equivalent thickness (t_{tex}) and the virtual thickness for the fabric modelling ($t_{m,SIM}$), i.e., $R = t_{m,SIM}/t_{tex}$. Hence, the Young's modulus (E_m) and maximum tensile strength (σ_m^{ult}, calculated from the maximum tensile force, F_m^{ult} and equivalent thickness, t_{tec}) were modified by dividing their values by the ratio *R*, as summarised in Table 6.

Finally, the required mesh connection length was assumed to be 100 mm (this was experimentally verified in previous studies, see [24]). Therefore, it was not necessary to represent the mesh along all pipe sections but only at 100 mm before and after each potential cracking plane. Hence, the mesh contribution moved to the concept of key elements, as represented in Figure 4a. The shear strength of the mesh/matrix interface was calculated to satisfy this hypothesis, assuming that the total contact area between the virtual fabric and the surrounding matrix could withstand the maximum tensile strength of the fabric. The calculated virtual tangential strength is summarised in Table 6.

	t_{tex} (mm)	$t_{m,SIM}$ (mm)	R	E_m (GPa)	$E_{m,SIM}$ (GPa)	σ_m^{ult} (MPa)	$\sigma_{m,SIM}^{ult}$ (MPa)	τ_{SIM} (MPa)
Cf	0.047	0.5	10.64	69.7	6.6	1255	118.0	0.8
GF	0.115	2.0	17.39	70.1	4.0	806	46.4	0.6
CF	0.045	2.0	44.44	236.1	5.3	1794	40.4	0.4

Table 6. Virtual mechanical properties for numerical simulation of fabric-increased virtual thickness.

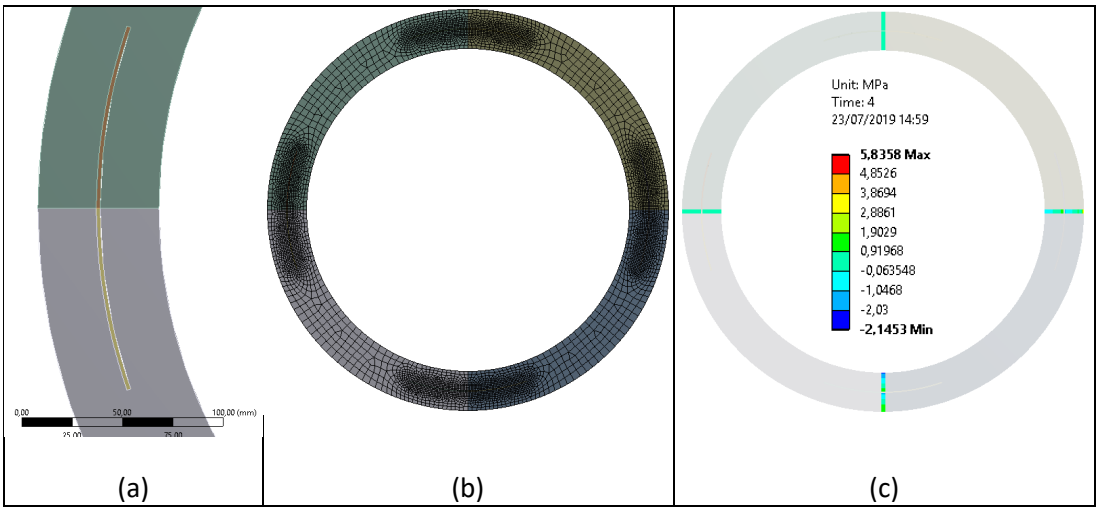

Figure 4. (a) Geometry simplification, (b) mesh used in calculations and (c) contact pressure at cracking of CGF specimen

2.5.2. Materials and contacts

The matrixes (mortar and concrete) were defined as elastic-perfect plastic in compression. This simplification of the real behaviour was previously used in similar structures (see [45]) under the assumption that the tensile response dominated the failure process. For the pipes studied, the post-crushing response was insignificant for the intended analysis. The fabrics were defined as linear elastic in tension. The geometric definition of the model guaranteed that the simulated parts of the fabrics were always subjected to tensile forces. Both the matrix and fabric tensile failures were defined using cohesive zone models in the corresponding contact areas, which were debonding models with energy. These models required the tensile strength and the corresponding fracture energy (1 Nm). Finally, a cohesive zone model was implemented for the tangential fabric–matrix interface response. To represent the brittle tensile failure of the fabric and matrix, little fracture energy was defined (1 Nm) in both cases. Similarly, little tangential fracture energy (1 Nm) was defined for the matrix–fabric interface.

The material properties summarised in Table 1 and 6 were used directly in the numerical simulation.

2.5.3. Boundary conditions and output data

All pipes were simply supported at the bottom point and loaded with an imposed vertical descending displacement at the top point. Additionally, lateral restrained concrete pipes were modelled by restraining the horizontal displacement of the nodes corresponding to the mid-height external face position.

Cracking force is defined as the reaction force at the vertical displacement application point when the matrix tensile strength (f_{ct}) is reached in any matrix–matrix contact area. The maximum load-bearing capacity of the pipe is defined as the reaction force at the vertical displacement application point when the maximum equivalent stress in the model is reached. This assumption allows a certain plasticisation of the matrix in compression but neglects post-critical analysis. Post-critical calculated response was not considered because of the simplifying hypothesis regarding the material definition.

2.5.4. General model summary

All models were 2D plain stress models using only bi-dimensional quadrilateral elements (PLANE183) and contact elements (CONTA172 and TARGE169). The numbers of elements and nodes are summarised in Table 7.

Model	***# 2D elements***	***# contact elements***	***# Total elements***	***# nodes***
M0	4609	---	4609	14599
MCf	6597	2624	9221	21477
C0	4243	---	4243	13591
CGF & CCF	6066	2848	8914	19994

Table 7. Summary of the model's metrics

3. Results

The experimental, analytical, and numerical simulation results of the cracking load (F_{fis}) and maximum load-bearing capacity (F_{max}) of each studied pipe are summarised in Table 8, together with the corresponding relative errors with respect to the experimental data ($E_{fis}^{ANA}, E_{max}^{ANA}, E_{fis}^{SIM}, E_{max}^{SIM}$). Table 3 provides more detailed results for each experimental test. For *M0* and *MCf* specimens, the average between the two experimental results from each case are presented for comparison purposes.

	Experimental		***Analytical***				***Simulation***			
Specimen	F_{fis}^{EXP} ***(N)***	F_{max}^{EXP} ***(N)***	F_{fis}^{ANA} ***(N)***	F_{max}^{ANA} ***(N)***	E_{fis}^{ANA} ***(%)***	E_{max}^{ANA} ***(%)***	F_{fis}^{SIM} ***(N)***	F_{max}^{SIM} ***(N)***	E_{fis}^{SIM} ***(%)***	E_{max}^{SIM} ***(%)***
M0	1843	1843	1516	1829	-17.7	-0.8	848	1666	-54.0	-9.6
MCf	1735	1832	1516	1914	-12.6	4.5	655	2100	-62.2	14.6
C0	30095	56044	27707	43399	-7.9	-22.6	24438	43233	-18.8	-22.9
CGF	21286	98366	27936	81150	31.2	-17.5	19600	94452	-7.9	-4.0
CCF	30318	93108	27056	87781	-10.8	-5.7	16414	94694	-45.9	1.7

Table 8. Summary of the experimental, analytical, and numerical results for the cracking and maximum loads

3.1. Experimental results

The force–displacement curves resulting from the experimental tests are shown in Figure 5.

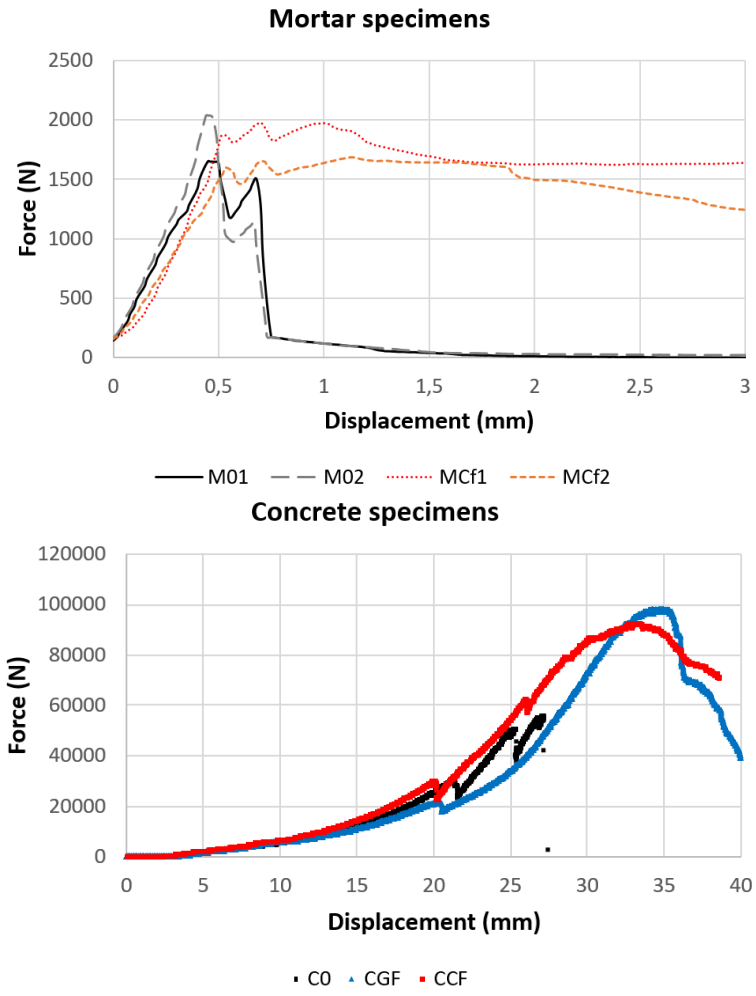

Figure 5. Force–displacement curves for mortar pipes (top) and concrete pipes (bottom)

Regarding the failure mode, all unreinforced pipes failed by the opening of four cracks, which caused the brittle failure of the structure (see Figure 6a and 6c). However, the four cracks should not open simultaneously but in pairs. Theoretically, the top/bottom pair of cracks should open at the intrados of the pipe first, and the second pair of cracks at the extrados of the pipe at the mid-height at a higher load, which cause the failure of the structure. This two-phase crack opening process is clearly observed in the results from the experiments on reinforced mortar pipes (*MCf1* and *MCf2*) and concrete pipes. However, the unreinforced mortar pipes showed a second force peak at a lower force than the first one. Finally, it was observed that the second pair of cracks did not appear simultaneously in the control concrete pipe (*C0*) test.

Regarding the failure mode, the unreinforced specimens (mortar and concrete matrixes) showed brittle failure with the instantaneous descend of the load (see Figure 5 and Figure 6), whereas the reinforced pipes showed a maintained load for the case of mortar pipes and a slowly descending load for the cases of reinforced concrete pipes.

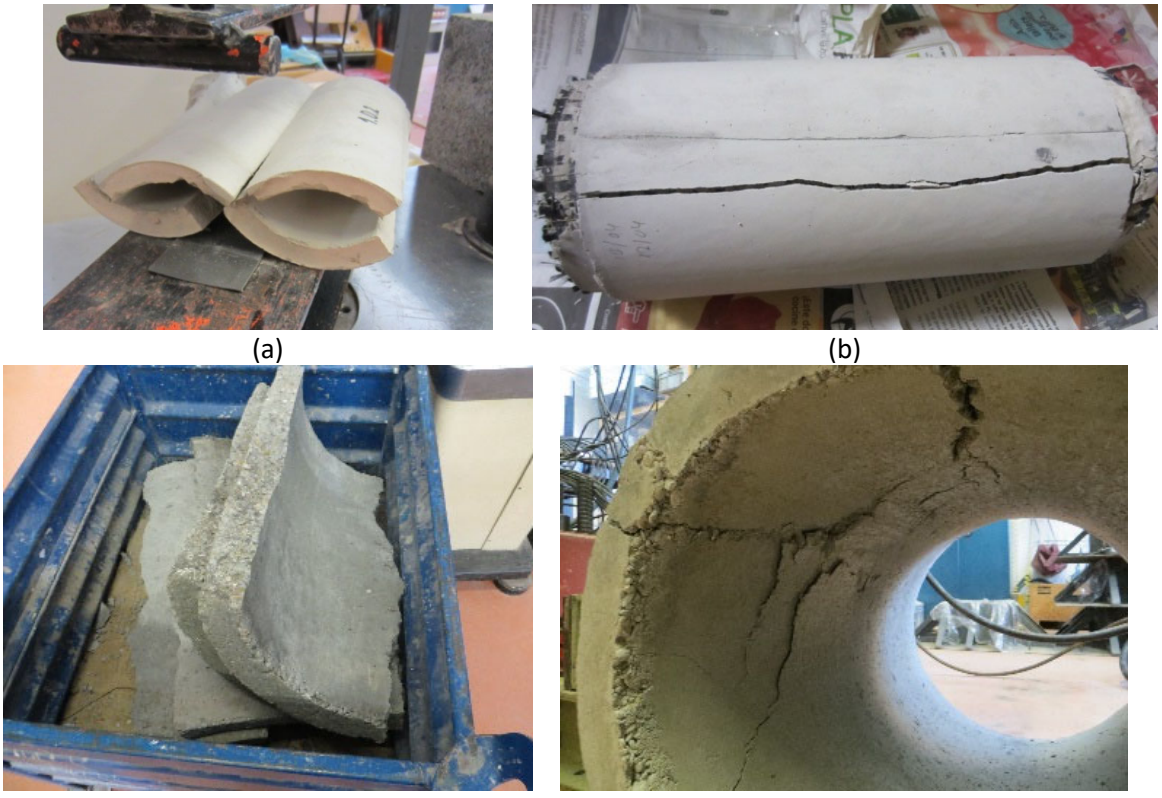

(a) (b)

(c) (d)

Figure 6. Specimens M01 (a), MCf1 (b), C0 (c), and CGF (d) after failure

Regarding the mortar pipes, the reinforcing fabric contributed to more energy dissipation, but the maximum resisted load was similar to those of the unreinforced cases. By contrast, the fabric contribution increased the maximum load-bearing capacity of the concrete pipes. Both cases failed by matrix crushing after crack opening (see Figure 6b and 6d).

3.2. Analytical results

According to the analytical results, all unreinforced specimens failed because of crack formation. By contrast, all reinforced pipes would have failed because of reaching the maximum

compressive strength of the matrix except specimen *CCF*. In this case, the analytical results indicated the tensile failure of the carbon fabric at a load of 62527 N. However, this type of failure was not observed experimentally. Instead, concrete crushing was observed in this particular test. The maximum load under concrete crushing hypothesis would have been 87781 N according to the proposed analytical approach. Hence, this value was used for further discussions of *CCF* analytical calculations.

According to the analytical results, the maximum load of the unreinforced mortar pipes was 20.6% higher than the corresponding first cracking load. This difference increased up to 56.6% for the concrete (*C0*) case.

3.3. Numerical results

All numerical simulations were performed in an Intel® Core™ i5-7500 CPU @ 3.40 GHz with 8 GB RAM memory running Windows 10 and lasted between 10 and 15 min.

According to the simulation results, the first crack always appeared in the top/bottom sections (see Figure 4c) and corresponded to reaching the matrix tensile strength (f_{ct}). Similarly, the maximum load-bearing capacity was set at the time in which the relative maximum of the von Mises equivalent stress was attained. It always indicated matrix crushing at the top/bottom extrados. Neither fabric tensile failure nor fabric sliding was predicted by the numerical simulation.

4. Discussion

First, it is noteworthy that only one specimen for each type of concrete pipe was experimentally tested. Hence, this must be considered in the following discussion.

Regarding the experimental results, it was observed that including the carbon fabric into the mortar pipes did not increase their strength. Hence, for this particular material and geometric definition, it appeared that the maximum load was primarily controlled by the mortar matrix. However, based on the full mechanical response during the test (Figure 5, top), it was clear that the fabric contributed to the post-critical ductile response of the structure dissipating significantly more energy than the unreinforced mortar pipes while maintaining significant strength for large deformations. For the unreinforced mortar pipes, two pics were observed in the force–displacement curve, which corresponded to the formation of two theoretical pairs of hinges. However, in contrast to the analytical results, a second peak (which corresponded to the lateral hinges in both the experimental and analytical results) was observed at a lower load than the first one. This may be owing to second-order effects and the additional deformation of the pipe after the first pair of hinges appeared.

The CF reinforced mortar pipes indicated (Figure 5, top) three maximum peaks. The first two corresponded to the formation of two pairs of hinges, whereas the last one reflected the additional strength contribution of the CF, which was mobilised after cracking. This maximum corresponded to the delamination load when the mortar and fabric separated, as observed experimentally.

Based on the experimental response of the concrete pipes (Figure 5, bottom), it is clear that including the reinforcing fabrics increased the load-bearing capacity of the concrete pipe. Nevertheless, the first concrete cracking load was similar among the three tested cases, indicating that before cracking, the concrete matrix primarily controlled the mechanical response of the pipes. However, from this point and on the fabrics start to influence the structural response of the pipe. Subsequently, the second pair of cracks started at a higher load for the reinforced concrete specimens than the control one. Hence, the third and fourth cracks

were formed at 51075 kN and 56044 kN, respectively, for specimen *C0*. In this case, these cracks at lateral positions were not formed simultaneously, likely because of particular asymmetries. By contrast, the third and fourth hinges were observed at 62667 kN and 87514 kN, respectively, for the *CCF* specimen and these were formed simultaneously at 94806 kN for the *CGF* specimen, which is close to the maximum load-bearing capacity of the specimen. These results may indicate that the GF is more likely to compensate for asymmetries through its larger deformability in comparison with the CF. Having more distributed efforts contributed to the mobilisation of more volume in the failure process; therefore, a higher load-bearing capacity was attained for the *CGF* case. Reaching a symmetric response with the simultaneous formation of third and fourth hinges is typically associated with a significantly higher load-bearing capacity, as shown in the presented data. All these cracking loads were obtained from data analysis and corresponded to the relative maximum loads recorded before the force decreased to at least 1 kN during the displacement-controlled test. Most of them were obvious because of their greater force decrease, as shown in Figure 5.

Comparing the experimental and analytical results, it was observed that the analytical model tended to underestimate the first cracking load (except the *CGF* case) and the maximum load bearing capacity (except the *MCf* case), thereby yielding conservative results. However, the average relative errors (without considering sign) of the first crack and ultimate load were 16.0% and 10.2%, respectively, which shows good agreement. These results indicated that for both structural configurations considered, the pure diametral compression for mortar pipes and the diametral compression with lateral restraints for concrete pipes, they were representative of the structural problem and the comparison criteria (reaching tensile strength and ultimate matrix crushing) was also.

Regarding the case of *CCF*, whose analytical predicted failure mode was fabric tensile failure (at 62527 kN, see section 3.2), it was observed that the calculations assuming the real observed failure mode (matrix crushing at 87781 kN) yielded better results. A possible justification for this mismatch would be that the curved specimens might have developed a higher fabric strength than those obtained from direct tensile tests because of the better load distribution among tows caused by the continuous re-adaptation of the load direction over the pipe wall curvature. However, evidence to prove this point is insufficient apart from that of the considered fabrics (CF for concrete specimens) developing significantly more strength than expected causing a change from the predicted failure mode to the observed one.

Comparing the experimental and simulation results, it was observed that the numerical results tended to underestimate (37.8% relative error) the first cracking load of all pipes, especially those with a mortar matrix (58.1% relative error) in comparison with the concrete ones (24.2% relative error). These differences appear to be related to the definition of matrix properties. In particular, the cohesive zone model defined between matrix parts, which used the tensile strength and the fracture energy data, may not be sufficiently accurate. Among these two parameters, the tensile strength is the most likely to have caused the difference between the simulated and experimental cracking loads as it controls the cracking stress, whereas the fracture energy primarily controls the post-cracking response of the cracked joint. Using values close to the flexural tensile strength of the matrixes may yield results that are closer to the experimental data. However, the direct tensile strength calculated from the compressive strength was used in the numerical simulations to ensure coherence with the cracking criteria defined for the analytical method to compare the two approaches. Nevertheless, it is noteworthy that the simulated cracking loads were always conservative; therefore, they may be used as design points with confidence.

To clearly demonstrate the effect of f_{ct} on the cracking load calculation using the finite element model, secondary calculations were conducted. When the calculation value of the tensile strength of concrete was increased up to 3 MPa (satisfying the general rule of using 10% of the compressive strength), the average error reduced from 24.2% to 3.3%. Similarly, when the calculation tensile strength of mortar was increased up to 5 MPa (value provided by mortar producer), the average error on the cracking load reduced from 58.1% to 15.9%. Hence, it is clear the model may justify the experimental results if other hypotheses of the tensile strength of matrixes had been used. Nevertheless, the values provided in Table 1 were used in this study to ensure coherence with previous analytical calculations and because of the better justified approach of using an existing formulation in a recognised standard.

The load-bearing capacity predicted by the simulations was close to the experimental one. An average underestimation of 4% (considering sign) and a relative error of 10.6% (not considering sign) were obtained. Similar accuracies were attained for the mortar and concrete pipes. As mentioned previously, the maximum load-bearing capacity criterion was associated with reaching the compressive strength of the matrix. Hence, the proper experimental characterisation of the matrixes' compressive strength can explain the final accuracy of the model predicting the ultimate capacity when the matrix crushing failure is the dominant mode. By contrast, the calculated approximation of the tensile strength may have caused the greater error of the cracking load.

Moreover, it is noteworthy that the same input parameters obtained from the minimum possible material information were used to compare the analytical and simulation results, although the second approach required significantly more parameters, which were calculated from the unique input parameters. It was observed that the proposed analytical method yielded more accurate results than the proposed numerical simulation approach. However, this

advantage of the analytical model over the numerical simulation was primarily associated with the calculation of the cracking load, whereas the load-bearing capacity obtained by both methods showed similar accuracies (10.2% error for analytical model and 10.6% error for simulation method). These results support the well-known idea that using complex numerical simulation tools necessitates a precise definition of the input variables to achieve accurate results.

Finally, the proposed analytical method based on calculating the cracking and maximum loads associated with the expected pipe response modes may be sufficient for designing and verifying the structural capabilities of FRCM pipes, in which neither more complex formulations nor numerical simulations are required. This fact may ease the production of FRCM pipes.

5. Conclusions

FRCM pipe specimens with a single fabric layer centred at the wall thickness were produced at laboratory (with mortar matrix) and industrial (with dry concrete) scales to demonstrate the practical feasibility of FRCMs. The specimens were tested under diametral compression and the results obtained were compared with analytical and numerical approaches; the following conclusions were obtained:

- The experimental tests showed that all pipes cracked by the formation of two hinges at the intrados in diametral opposite points aligned with the applied load. The maximum load-bearing capacity was reached when the matrix crushed at the same points after cracking occurred at the mid-height lateral sections of the pipes. Neither fabric sliding nor fabric tensile failure was observed.

- The analytical approach showed accurate results for both the cracking load (16.0% relative error) and load-bearing capacity (10.2% relative error). Therefore, it was proven as an efficient tool for designing the proposed innovative FRCM pipes.
- The numerical simulations yielded accurate load-bearing capacity results (10.6% relative error) based on the experimentally determined compressive strength. However, when using calculation-derived properties for the calculation of the cracking load, the models' accuracy decreased significantly (37.8% relative error). Using more accurate tensile strength values would increase the model accuracy in predicting the cracking load.

In conclusion, producing FRCM pipes is technologically feasible, and the calculations involved can be performed using simple analytical tools.

Acknowledgements

The authors gratefully acknowledge the support of SORIGUÉ S.A. in the development of the project TUBOTEX. The first author is a Serra Húnter Fellow. The second author acknowledges the Ministry of Education Science and Technology (Mesyt) of the Dominican Republic for financial support through its international scholarship program.

Funding

This research was partially funded by the company SORIGUÉ S.A. for the development of the project TUBOTEX, which was partially funded by the Spanish government (CDTI).

References

[1] T. Gardiner, B. Currie, Flexural behaviour of composite cement sheets using woven polypropylene mesh fabrics, Int. J. Cem. Compos. Light. Concr. 5 (1983) 193–197. doi:10.1016/0262-5075(83)90006-4.

[2] E. Bernat, L. Gil, P. Roca, C. Escrig, Experimental and analytical study of TRM strengthened brickwork walls under eccentric compressive loading, Constr. Build. Mater. 44 (2013) 35–47. doi:http://dx.doi.org/10.1016/j.conbuildmat.2013.03.006.

[3] J. Harajli, M.H., ELKhatib, H., Tomas San-Jose, Masonry Walls Strengthened Using Fibre Textile-Mortar System: Experimental Evaluation of Out-of-Plane Cyclic Response, in: CSHM-3, Ottawa-Gatineau, Canada, 2010: pp. 19–32.

[4] A. Cascardi, F. Micelli, M.A. Aiello, FRCM-confined masonry columns: experimental investigation on the effect of the inorganic matrix properties, Constr. Build. Mater. (2018). doi:10.1016/j.conbuildmat.2018.08.020.

[5] A. Bilotta, F. Ceroni, E. Nigro, M. Pecce, Experimental tests on FRCM strengthening systems for tuff masonry elements, Constr. Build. Mater. (2017). doi:10.1016/j.conbuildmat.2017.01.124.

[6] C. Escrig, L. Gil, E. Bernat-Maso, F. Puigvert, Experimental and analytical study of reinforced concrete beams shear strengthened with different types of textile-reinforced mortar, Constr. Build. Mater. 83 (2015) 248–260. doi:10.1016/j.conbuildmat.2015.03.013.

[7] D. Marcinczak, T. Trapko, M. Musiał, Shear strengthening of reinforced concrete beams with PBO-FRCM composites with anchorage, Compos. Part B Eng. (2019). doi:10.1016/j.compositesb.2018.09.061.

[8] N. Ismail, T. El-Maaddawy, N. Khattak, Quasi-static in-plane testing of FRCM strengthened non-ductile reinforced concrete frames with masonry infills, Constr. Build. Mater. (2018). doi:10.1016/j.conbuildmat.2018.07.230.

[9] O. Awani, T. El-Maaddawy, N. Ismail, Fabric-reinforced cementitious matrix: A promising strengthening technique for concrete structures, Constr. Build. Mater. 132 (2017) 94–111. doi:10.1016/j.conbuildmat.2016.11.125.

[10] D. Arboleda, F.G. Carozzi, A. Nanni, C. Poggi, Testing Procedures for the Uniaxial Tensile Characterization of Fabric-Reinforced Cementitious Matrix Composites, J. Compos. Constr. 20 (2016) 04015063. doi:10.1061/(ASCE)CC.1943-5614.0000626.

[11] RILEM Technical Committee 232-TDT (Wolfgang Brameshuber), W. Brameshuber, M. Hinzen, A. Dubey, A. Peled, B. Mobasher, A. Bentur, C. Aldea, F. Silva, J. Hegger, T. Gries, J. Wastiels, K. Malaga, C. Papanicolaou, L. Taerwe, M. Curbach, V. Mechtcherine, A. Naaman, J. Orlowsky, P. Hamelin, H.W. Reinhardt, S. Shah, R. Toledo, T. Triantafillou, A. Si Larbi, D. Garcia, L. Garmendia, S. Gopinath, F. Jesse, Recommendation of RILEM TC 232-TDT: test methods and design of textile reinforced concrete: Uniaxial tensile test: test method to determine the load bearing behavior of tensile specimens made of textile reinforced concrete, Mater. Struct. Constr. 49 (2016) 4923–4927. doi:10.1617/s11527-016-0839-z.

[12] S. De Santis, G. De Felice, Tensile behaviour of mortar-based composites for externally bonded reinforcement systems, Compos. Part B Eng. 68 (2015) 401–413. doi:10.1016/j.compositesb.2014.09.011.

[13] A. Peled, A. Bentur, Fabric structure and its reinforcing efficiency in textile reinforced cement composites, Compos. Part A Appl. Sci. Manuf. 34 (2003) 107–118. doi:10.1016/S1359-835X(03)00003-4.

[14] M. El Messiry, A.-B. Mito, A. Al-Oufy, E. El-Tahan, Effect of fabric material and tightness on the mechanical properties of fabric–cement composites, Alexandria Eng. J. 53 (2014)

795–801. doi:10.1016/j.aej.2014.09.002.

[15] F. Han, H. Chen, K. Jiang, W. Zhang, T. Lv, Y. Yang, Influences of geometric patterns of 3D spacer fabric on tensile behavior of concrete canvas, Constr. Build. Mater. 65 (2014) 620–629. doi:10.1016/j.conbuildmat.2014.05.041.

[16] A. PELED, B. MOBASHER, Brittle Matrix Composites 7, Elsevier, 2003. doi:10.1533/9780857093103.505.

[17] A. Peled, Z. Cohen, Y. Pasder, A. Roye, T. Gries, Influences of textile characteristics on the tensile properties of warp knitted cement based composites, Cem. Concr. Compos. 30 (2008) 174–183. doi:10.1016/j.cemconcomp.2007.09.001.

[18] A. Peled, B. Mobasher, Z. Cohen, Mechanical properties of hybrid fabrics in pultruded cement composites, Cem. Concr. Compos. 31 (2009) 647–657. doi:10.1016/j.cemconcomp.2009.06.002.

[19] E. Butnariu, A. Peled, B. Mobasher, Brittle Matrix Composites 8, Elsevier, 2006. doi:10.1533/9780857093080.293.

[20] M. Krüger, H.-W. Reinhardt, M. Fichtlscherer, Bond behaviour of textile reinforcement in reinforced and prestressed concrete, Otto-Graf-Journal. 12 (2001) 33–50.

[21] S. Xu, H. Li, Bond properties and experimental methods of textile reinforced concrete, J. Wuhan Univ. Technol. Mater. Sci. Ed. 22 (2007) 529–532. doi:10.1007/s11595-006-3529-9.

[22] A. Peled, Pre-tensioning of fabrics in cement-based composites, Cem. Concr. Res. 37 (2007) 805–813. doi:10.1016/j.cemconres.2007.02.010.

[23] S. Gopinath, R. Gettu, N.R. Iyer, Influence of prestressing the textile on the tensile behaviour of textile reinforced concrete, Mater. Struct. Constr. 51 (2018) 1–12. doi:10.1617/s11527-018-1194-z.

[24] E. Bernat-maso, L. Gil, L. Mercedes, C. Escrig, Mechanical properties of pre-stressed fabric-reinforced cementitious matrix composite (PFRCM), Constr. Build. Mater. 191 (2018) 228–241. doi:10.1016/j.conbuildmat.2018.09.210.

[25] V. Mechtcherine, High performance Cement-based Composites. Textile Reinforced Concrete (TRC), (2011) 1–48.

[26] T. Quadflieg, Y. Goldfeld, G. Dittel, T. Gries, New Age Advanced Smart Water Pipe Systems Using Textile Reinforced Concrete, Procedia Manuf. 21 (2018) 376–383. doi:10.1016/j.promfg.2018.02.134.

[27] A. Peyvandi, P. Soroushian, S. Jahangirnejad, Enhancement of the structural efficiency and performance of concrete pipes through fiber reinforcement, Constr. Build. Mater. 45 (2013) 36–44. doi:10.1016/j.conbuildmat.2013.03.084.

[28] W. Brameshuber, Textile reinforced concrete multi-layer composite pipes, in: Ibac RWTH Aachen University (Ed.), Text. Reinf. Concr. Rep. 36 Text. Reinf. Concr. - State-of-the-Art Rep. RILEM TC 201-TRC, RILEM Publ. SARL, Aachen, Germany, 2006: pp. 263–266. https://books.google.es/books?id=nV4JmLPlqV0C.

[29] U. HELBIG, M. LIEBOLDT, T. ENGLER, M. WALDMANN, DE102007038932 (A1) - Textile-matrix-laminate for manufacturing reinforced component parts i.e. multi-layer laminate pipe, has lattice-like narrow textile i.e. thread layer sewing substance, embedded in matrix such as fine concrete matrix, DE102007038932 (A1), 2009.

[30] ACI Committee 549, ACI 549.4R-13 - Guide to design and construction of externally bonded fabric-reinforced cementitious matrix (FRCM) systems for repair and strengthening concrete and masonry structures, (2013).

[31] J. Aveston, A. Kelly, Theory of multiple fracture of fibrous composites, J. Mater. Sci. 8 (1973) 352–362. doi:10.1007/BF00550155.

[32] E. Grande, G. Milani, Interface modeling approach for the study of the bond behavior of FRCM strengthening systems, Compos. Part B. 141 (2018) 221–233. doi:10.1016/j.compositesb.2017.12.052.

[33] E. Bertolesi, F.G. Carozzi, G. Milani, C. Poggi, Numerical modeling of Fabric Reinforce Cementitious Matrix composites (FRCM) in tension, Constr. Build. Mater. 70 (2014) 531–548. doi:10.1016/j.conbuildmat.2014.08.006.

[34] N. Williams Portal, K. Lundgren, A.M. Walter, J.O. Frederiksen, L.N. Thrane, Numerical modelling of textile reinforced concrete, in: Proc. 8th Int. Conf. Fract. Mech. Concr. Concr. Struct. Fram. 2013, 2013: pp. 886–897. http://www.scopus.com/inward/record.url?eid=2-s2.0-84879893673&partnerID=tZOtx3y1.

[35] C. Carloni, T. D'Antino, L.H. Sneed, C. Pellegrino, Three-Dimensional Numerical Modeling of Single-Lap Direct Shear Tests of FRCM-Concrete Joints Using a Cohesive Damaged Contact Approach, J. Compos. Constr. 22 (2018) 04017048. doi:10.1061/(ASCE)CC.1943-5614.0000827.

[36] H.M. Elsanadedy, T.H. Almusallam, S.H. Alsayed, Y.A. Al-Salloum, Flexural strengthening of RC beams using textile reinforced mortar – Experimental and numerical study,

Compos. Struct. 97 (2013) 40–55. doi:10.1016/j.compstruct.2012.09.053.

[37] Y.A. Al-Salloum, H.M. Elsanadedy, S.H. Alsayed, R.A. Iqbal, Experimental and Numerical Study for the Shear Strengthening of Reinforced Concrete Beams Using Textile-Reinforced Mortar, J. Compos. Constr. 16 (2012) 74–90. doi:10.1061/(ASCE)CC.1943-5614.0000239.

[38] F. Schladitz, M. Frenzel, D. Ehlig, M. Curbach, Bending load capacity of reinforced concrete slabs strengthened with textile reinforced concrete, Eng. Struct. 40 (2012) 317–326. doi:10.1016/j.engstruct.2012.02.029.

[39] C. Menna, D. Asprone, M. Durante, A. Zinno, A. Balsamo, A. Prota, Structural behaviour of masonry panels strengthened with an innovative hemp fibre composite grid, Constr. Build. Mater. 100 (2015) 111–121. doi:10.1016/j.conbuildmat.2015.09.051.

[40] F.G. Carozzi, G. Milani, C. Poggi, Mechanical properties and numerical modeling of Fabric Reinforced Cementitious Matrix (FRCM) systems for strengthening of masonry structures, Compos. Struct. 107 (2014) 711–725. doi:10.1016/j.compstruct.2013.08.026.

[41] G.P. Lignola, A. Bilotta, F. Ceroni, Assessment of the effect of FRCM materials on the behaviour of masonry walls by means of FE models, Eng. Struct. (2019). doi:10.1016/j.engstruct.2019.01.035.

[42] CEN, European Standard EN 13813:2002. Screed material and floor screed - screed material - properties and requirements, (2002).

[43] CEN, European Standard EN 12350-2:2009, Testing fresh concrete. Part 2: Slump- test, (2009).

[44] Ministerio de Fomento. Comisión Permanente del Hormigón, EHE-08. Instrucción de Hormigón Estructural, (2008).

[45] E. Bernat-Maso, L. Gil, P. Roca, Numerical analysis of the load-bearing capacity of brick masonry walls strengthened with textile reinforced mortar and subjected to eccentric compressive loading, Eng. Struct. 91 (2015). doi:10.1016/j.engstruct.2015.02.032.